Supplement of

Atmospheric new particle formation in the eastern region of China: a mechanistic investigation at multiple sites

Jiaqi Jin et al.

Correspondence to: Lin Wang (lin wang@fudan.edu.cn)

Data analysis

New particle formation (NPF) events were selected, based on the characteristics of particle size distributions (PSDs), when the following two conditions are met: (1) A significant increase in the number concentration of particles with diameters less than 25 nm. The upper size limit of 25 nm is defined, because nucleation events may occur at a certain distance from the observation station in some cases. By the time new particles are detected, their size may have already grown to 25 nm or even larger. (2) The formation and growth of nucleation modes of particles last for at least one hour, and a banana-shaped PSD need to be observed. If the second point is not met, it suggests that the particle formation event is non-regional and may originate from point or line sources of nanoparticles.

Particle formation rate quantifies the growth flux at a specific particle diameter. It was calculated using a balance formula developed by Cai and Jiang (Cai and Jiang, 2017), which offers an improved accuracy in estimating coagulation scavenging under conditions of elevated aerosol loading:

$$J_k = \frac{dN_{[d_k\,,\,d_u)}}{dt} + \sum_{d_g = d_k}^{d_{u-1}} \sum_{d_i = d_{\min}}^{+\infty} \beta_{(i,g)}\, N_{[d_i\,,\,d_{i+1})} N_{[d_g\,,\,d_{g+1})}$$

$$-\frac{1}{2} \sum_{d_g = d_{\min}}^{d_{u-1}} \sum_{d_i^3 = \max\left(d_{\min}^3\,,\, d_k^3 - d_{\min}^3\right)}^{d_{i+1}^3 + d_{g+1}^3 \leq d_u^3} \beta_{(i,g)}\, N_{[d_i\,,\,d_{i+1})} N_{\left[d_g\,,\,d_{g+1}\right)} + n_u \mathrm{GR}_u \tag{S1}$$

where J_k is the formation rate of particles at size d_k (1.4 nm or 1.7 nm in this study); d_u is a calculated upper size bound selected according to different nucleation characteristics, and $d_{\min}$ is the lower limit of instrument measurement; N is defined as the total number concentration of particles in the corresponding subscript range, and β refers to the coagulation coefficient of two particle sizes; n is the particle size distribution function that equals $\mathrm{d}N/\mathrm{d}d_\mathrm{p}$; $\mathrm{GR_u}$ is the growth rate of the nearest particle size segment of d_u.

Condensation sink (CS) characterizes the condensing vapor sink caused by pre-existing aerosols and can be calculated using the following equation (Kulmala et al., 2013):

$$\mathrm{CS} = 2\pi \mathrm{D} \sum_{d_\mathrm{p}} \beta_{m,d_\mathrm{p}}\, N_{d_\mathrm{p}} \tag{S2}$$

where D represents the diffusion coefficient of the condensing vapor (SA), and $\beta_{m,dp}$ is the transitional regime correction factor.

The coagulation scavenging of particles was estimated through CS:

$$\mathrm{CoagS}_{d_p} = \mathrm{CS}\left(\frac{d_\mathrm{p}}{0.64}\right)^{-1.7} \tag{S3}$$

The volatility of oxygenated organic molecules (OOMs) can be estimated by the following formula (Mohr et al., 2019):

$$\log_{10} C^{*}\,(300\ \mathrm{K}) = (25 - \mathrm{n_C})\mathrm{b_C} - (\mathrm{n_O} - 3\mathrm{n_N})\mathrm{b_O} - \frac{2(\mathrm{n_O} - 3\mathrm{n_N})\mathrm{n_C}}{\mathrm{n_C} + \mathrm{n_O} - 3\mathrm{n_N}}\mathrm{b_{CO}} - \mathrm{n_N}\mathrm{b_N} \tag{S4}$$

where C^* is the saturation mass concentration of the molecule at 300 K, and $\mathrm{n_C}$, $\mathrm{n_O}$ and $\mathrm{n_N}$ represent molecular number of carbon, oxygen and nitrogen, respectively. $\mathrm{b_C}=0.475$; $\mathrm{b_O}=0.2$; $\mathrm{b_{CO}}=0.9$; $\mathrm{b_N}=2.5$. In different ambient temperatures ranging from 260 to 310 K, the enthalpy of evaporation ($\triangle \mathrm{H_{vap}}$) should be considered (Donahue et al., 2011):

$$C^{*}(\mathrm{T}) = C^{*}(300\ \mathrm{K})\exp\left(\frac{\triangle \mathrm{H_{vap}}}{R}\left(\frac{1}{300\ \mathrm{K}} - \frac{1}{T}\right)\right) \tag{S5}$$

where R is the gas constant, T is the temperature in Kelvin, and $\triangle \mathrm{H_{vap}}$ is the vaporization enthalpy, which was calculated by

(Epstein et al., 2010):

$$\triangle \mathrm{H_{vap}} = -5.7 \log_{10} C^{*}(300\ \mathrm{K}) + 129 \tag{S6}$$

Introduction of modules in the cluster dynamics–multicomponent sectional model

In the cluster dynamics module, the evolution of clusters is described. Clusters with more than five sulfuric acid (SA) or dimethylamine (DMA) molecules are not included in the simulation. The collision rate coefficients between molecules and clusters were calculated by kinetic gas theory (Ortega et al., 2012). The evaporation rates of the clusters were derived from these collision rate coefficients and the cluster formation free energy were referenced from the literature (Olenius et al., 2017). The reported range of the Gibbs free energy of formation (△G) for SA_1DMA_1 at the standard temperature 298.15 K ranges from -11.0 to -15.4 kcal mol^{-1} based on different quantum chemistry models (Ortega et al., 2012; Myllys et al., 2019; Ge et al., 2020; Han et al., 2020). Here, It was set to be -13.5 kcal mol^{-1} at 298.15 K, according to the value from Myllys et al. (2019).

In the sectional module, the evolution of particle growth is depicted by the effects of condensation, evaporation, coagulation and loss. Particles were divided into bins in terms of their geometric diameters, from 1.1 nm to 115.9 nm. Each bin was further divided into two parts, which recorded the mass of SA-DMA cluster and OOMs, respectively. The particles in each bin are assumed to be totally mixed with these condensable species, meaning they share the same chemical composition. Theoretically, this module can simulate the initial growth of newly formed particles, thereby simulating $J_{1.7}$. The sectional module may not be practical, because simulated PSDs are beyond the model boundaries in some cases.

Because the sectional module focuses on the formation and growth of newly-formed particles, particles that are obviously not from new particle formation need to be excluded from the simulation. To address this, a variable simulation domain is set as a function of time within the PSD of each NPF event. This domain is defined through polynomial fitting to delineate the particle size range generated by NPF. Particles within the simulation domain undergo condensation, evaporation, and coagulation as described previously, while particles outside are pre-existing and contribute to the coagulation sink of particles within the domain. The simulation domain not only helps reduce computational costs, but also allows us to focus on NPF itself rather than the evolution of pre-existing or large primary particles. In some NPF events, the PSD simulations perform well (Figure S1a). However, in other cases, due to high concentrations of OOMs that lead to extreme high growth rates, particles generated by NPF quickly exceed the boundary of the simulation domain (Figure S1b). This causes a decrease on the simulated particle number concentration (N) beyond the critical size (k) when calculating particle formation rate (Equation S1), leading to smaller or even negative simulated nucleation rates. Even without setting a domain boundary, the model itself has a particle-size limit (115.9 nm), which are also exceeded by simulated particles (Figure S1c). However, if OOMs are not treated as condensable vapors and only the effect of SA and its clusters are considered, the simulated particles do not exceed the boundary (Figure S1d).

The deviation of scaled nucleation rate

The scaled process of particle formation rate is similar to that of SA dimer concentration. We firstly focus on the deviation of scaled $J_{1.4}$ ($J_{1.4,\mathrm{scaled}}$):

$$J_{1.4,\mathrm{scaled}} = J_{1.4,\mathrm{meas}} \cdot \mathrm{C}_{1.4}(\mathrm{CS_{median}}, [\mathrm{DMA}]_{\mathrm{med}}) \tag{S7}$$

where $J_{1.4,\mathrm{meas}}$ refers to the measured $J_{1.4}$; $\mathrm{C}_{1.4}$ ($\mathrm{CS_{median}}$, $[\mathrm{DMA}]_{\mathrm{median}}$) is defined as the scaling coefficient for $J_{1.4,\ \mathrm{meas}}$, and is calculated by:

$$\mathrm{C}_{1.4}(\mathrm{CS_{median}}, [\mathrm{DMA}]_{\mathrm{median}}) = \frac{J_{1.4,\mathrm{sim,median}}}{J_{1.4,\mathrm{sim}}} \tag{S8}$$

where $J_{1.4,\mathrm{sim}}$ is the simulated $J_{1.7}$, which is calculated by inputting measured data in the model; $J_{1.4,\mathrm{sim,median}}$ is the simulated $J_{1.4}$ with median inputs of CS and DMA concentration, [DMA], and is calculated by inputting measured SA monomer concentration ($[SA_1]$) and temperature, but the median [DMA] (2.3 pptv) and the median CS (0.017 s^{-1}) in all NPF events. $J_{1.4,\mathrm{sim,median}}$ can be regarded as the theoretical $J_{1.4,\mathrm{meas}}$ when measured [DMA] and CS reach the median values. A crucial assumption of this scaled method is that $J_{1.4,\mathrm{sim}}$ and $J_{1.4,\mathrm{meas}}$ are approximately equal.

Based on $J_{1.4}$, the scaled $J_{1.7}$ ($J_{1.7,\mathrm{scaled}}$) is deviated below:

$$
\begin{aligned}
J_{1.7,\mathrm{scaled}} &= J_{1.7,\mathrm{meas}} \cdot \mathrm{C}_{1.7}(\mathrm{CS}_{\mathrm{median}}, [\mathrm{DMA}]_{\mathrm{median}}, \mathrm{P}_{\mathrm{median}}) \\
&= J_{1.7,\mathrm{meas}} \cdot \frac{J_{1.7,\mathrm{sim,median}}}{J_{1.7,\mathrm{sim}}} \\
&= J_{1.7,\mathrm{meas}} \cdot \frac{J_{1.4,\mathrm{sim,median}} \cdot \mathrm{P}_{\mathrm{median}}}{J_{1.4,\mathrm{sim}} \cdot \mathrm{P}}
\end{aligned}
\tag{S9}
$$

where $J_{1.7,\mathrm{meas}}$ is the measured $J_{1.7}$; $\mathrm{C}_{1.7}$ ($\mathrm{CS}_{\mathrm{median}}$, $[\mathrm{DMA}]_{\mathrm{median}}$, $\mathrm{P}_{\mathrm{median}}$)is the scaling coefficient for $J_{1.7,\mathrm{meas}}$. $J_{1.7,\mathrm{sim}}$ is the simulated $J_{1.7}$; $J_{1.7,\mathrm{sim}}$ is the simulated $J_{1.7,\mathrm{sim}}$; $J_{1.7,\mathrm{sim,median}}$ is the simulated $J_{1.7}$ with median measured inputs, except for $[\mathrm{SA}_1]$ and temperature; P is the survival probability from 1.4 nm to 1.7 nm calculated by Equation 1; $\mathrm{P}_{\mathrm{median}}$ is the median P (0.67) in all NPF events.

The simulation of $J_{1.4}$

There is an acceptable consistency between $J_{1.4,\mathrm{meas}}$ and $J_{1.4,\mathrm{sim}}$ by considering the uncertainties (Figure S3). Their differences are basically within two orders of magnitude. This kind of difference is typically under one order of magnitude inside each previous indoor or outfield experiment (Kürten et al., 2018; Xiao et al., 2021), which is lower than the data in this study. A reasonable explanation could be the different range of uncertainties. For a single observation, the measurement uncertainty is relatively low (Freshour et al., 2014), and the resulting simulation uncertainty can be controlled within a narrow range. However, our measurement spans several years and involves multiple sites, and the uncertainty range of $J_{1.4}$ is likely to be amplified to a greater extent.

The uncertainty range of $J_{1.4,\mathrm{sim}}$ need to be analyzed basically. Overall, the output range spans approximately four orders of magnitude, indicating that the model is highly sensitive to inputs. Theoretically, particle formation rate is approximately proportional to $[\mathrm{SA}_1]^4$ in SA-DMA nucleation (Cai et al., 2021). This relationship is particularly evident under high CS and high [DMA]. Considering the uncertainty of $[\mathrm{SA}_1]$ (+100%/-50%) merely, the uncertainty of $J_{1.4,\mathrm{sim}}$ is estimated to be +1600%/-94%. Since there is no simple algebraic relation between [DMA] and $J_{1.4}$, their quantitative relation can be reflected from observational data. A study in urban areas suggested that $J_{1.4}$ roughly varies in proportion to twice of the change of [DMA] (1-5 pptv) in the same conditions (Cai et al., 2021). Considering the uncertainty of [DMA] (+150%/-60%) merely, the uncertainty of $J_{1.4,\mathrm{sim}}$ is estimated to be +400%/-80%. In short, by superimposing the uncertainty of measured precursors, the uncertainty of $J_{1.4}$ given by the model is numerically reasonable.

The volatility distribution of OOMs concentration

The volatility distribution of OOMs is shown in Figure S7. Merely OOMs with $\log10[C^*(\mu\mathrm{g\ m}^{-3})] \leq 0$, which are defined as condensable OOMs (Qiao et al., 2021), are included in the statistics. Condensable OOMs have been demonstrated to drive the growth of nanoparticles (Li et al., 2022), and even be capable of nucleating (Riccobono et al., 2014; Bianchi et al., 2016). Other OOMs with $\log10[C^*(\mu\mathrm{g\ m}^{-3})] > 0$, due to their negligible role in NPF events, are not considered in this study (Bianchi et al., 2016; Li et al., 2023). According to their different volatility range, condensable OOMs are classified as ultralow-volatility organic compounds (ULVOCs, $C^* \leq 3\times10^{-9}$ μg m^{-3}), extremely low-volatility organic compounds (ELVOCs, $3\times10^{-9} < C^* \leq 3\times10\text{-}5$ μg m^{-3}), low-volatility organic compounds (LVOCs, $3\times10^{-5} < C^* \leq 3\times10^{-1}$ μg m^{-3}), and a fraction of semi-volatile organic compounds (SVOCs, $3\times10^{-1} < C^* \leq 3\times10^{3}$ μg m^{-3}).

The effect of temperature on $J_{1.7}$

$J_{1.7,\mathrm{scaled}}$ also exhibits a strong temperature dependence (Figure S8) like $J_{1.4,\mathrm{scaled}}$ (Figure 6). $J_{1.7,\mathrm{sim}}$ improves substantially to almost the same level as the $J_{1.4,\mathrm{sim}}$ after accounting for growth rate of 1.4-1.7 nm particles ($\mathrm{GR}_{1.4\text{-}1.7}$) contributed by OOMs (Figure 7). The magnitude of P mainly depends on $\mathrm{GR}_{1.4\text{-}1.7}$ and CS, and is not directly related to temperature. Therefore, using the median P allows for scaling other factors to better reflect the relationship between $J_{1.7}$ and temperature. It is notice that temperature indirectly influences $\mathrm{GR}_{1.4\text{-}1.7}$ through three pathways. The first path is the effect on the process of condensation, primarily reflected in the collision rate between molecules and particles as well as the Kelvin effect (Troestl et al., 2016), which are minor and are considered by Equation 2. The second is the effect on the volatility of same kind of OOMs (Epstein et al., 2010), which is corrected by Equation S6. The third is that temperature could influence the oxidation rate of organics, and alter the number of effective oxygen of total OOMs to change their volatilities. This path involves the whole system of organic oxidation in the atmosphere, and is too complicated to be discussed here. The third effect has been identified to be weaker than the second one in a chamber research (Caudillo et al., 2021), and can be relatively neglected to some extent.

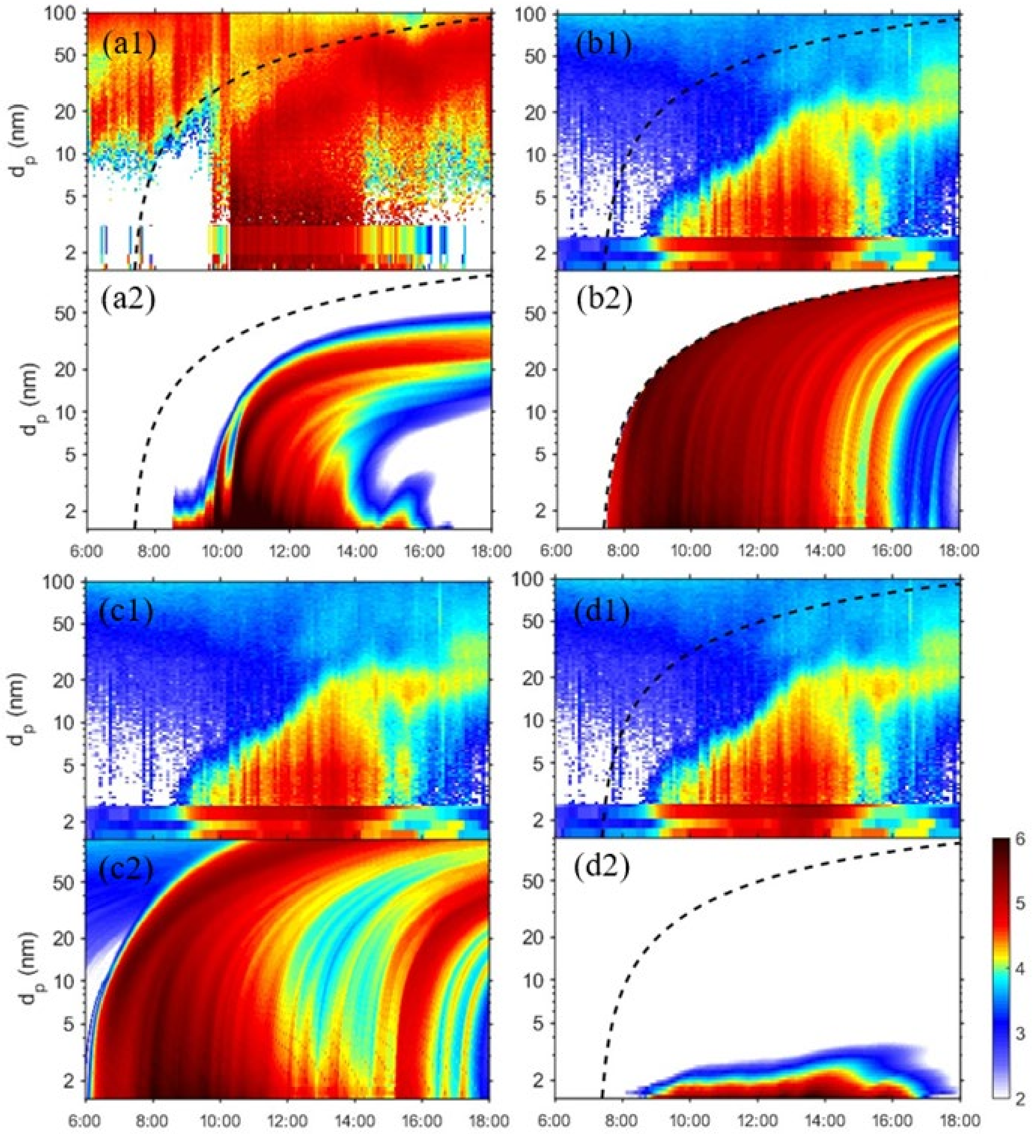

Figure S1: Comparison between the observation and simulation for two events. The color bar shows the log$_{10}$ values of the particle size distribution (dN = dlog$_{10}$$dp$ in units of cm^{-3}) (a) The NPF events on January 20th, 2019 at Wangdu, consists of (a1) the observed PSD and (a2) the simulated PSD considering both OOMs and the domain boundary. (b)-(d) The NPF events on January 27th, 2023 at Dianshan Lake. The observed PSDs are the same in (b1), (c1) and (d1). The simulated PSDs in (b)-(d) have different simulation settings: (b2) with OOMs and the domain boundary; (c2) with OOMs but without the domain boundary; (c2) without OOMs but with the domain boundary. The dashed curves are the upper boundary of the simulation domain for NPF.

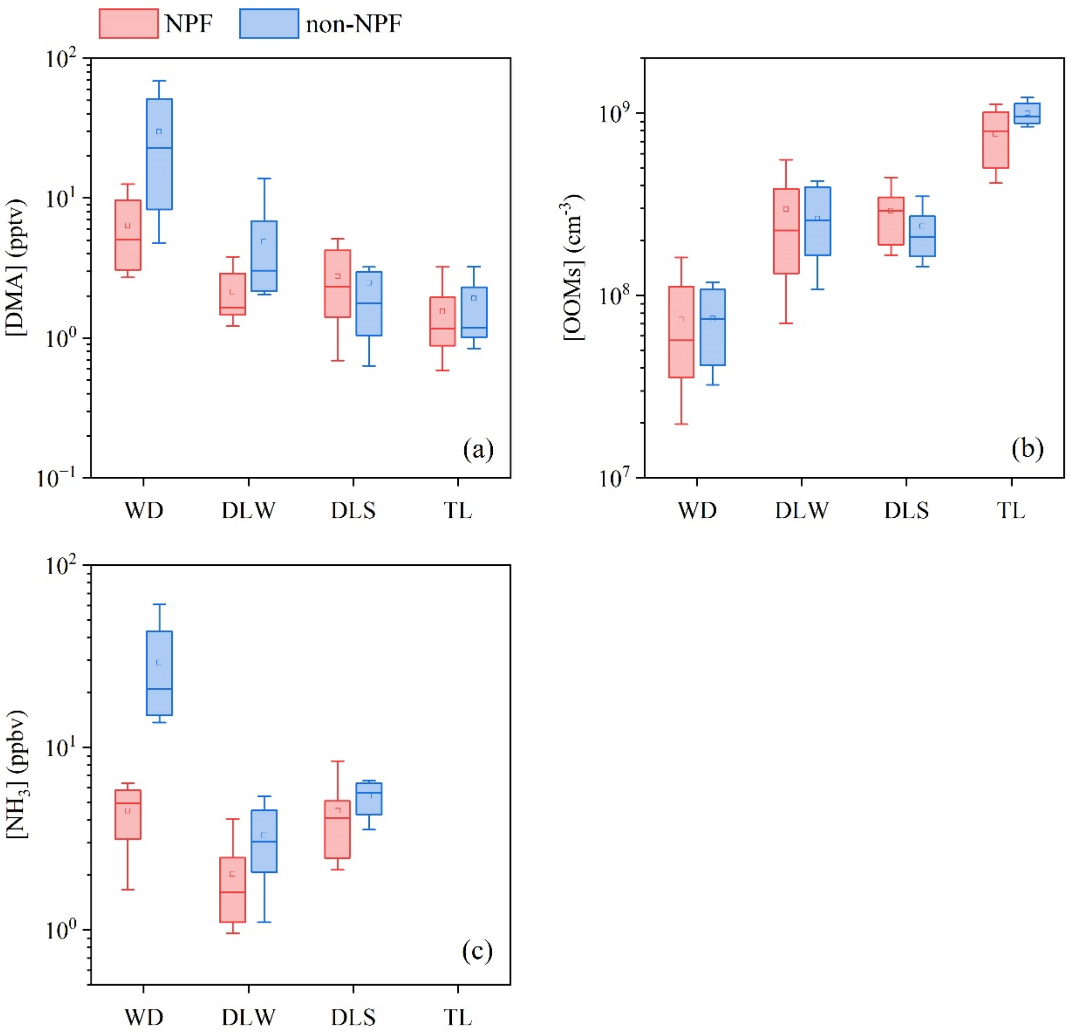

Figure S2: Parameters related to NPF: (a) [DMA], (b) OOMs concentration ([OOMs]) and (c) NH$_3$ concentration ([NH$_3$]) during NPF periods and non-NPF periods. The NPF period is defined as the period with the maximum value of $J_{1.7}$ in each NPF event, and the non-NPF period is defined as the median range of all NPF periods (9:00-11:00) in non-NPF days. In order to eliminate the influence of precipitation, only sunny and cloudy days are selected for non-NPF. The transverse lines and square markers inside the boxes indicate mean values and median values, respectively. The bottom and top edges of the box indicate the 25th and 75th percentiles, respectively. The bottom and top edges of the whisker lines outside of the boxes indicate the 10th and 90th percentiles, respectively.

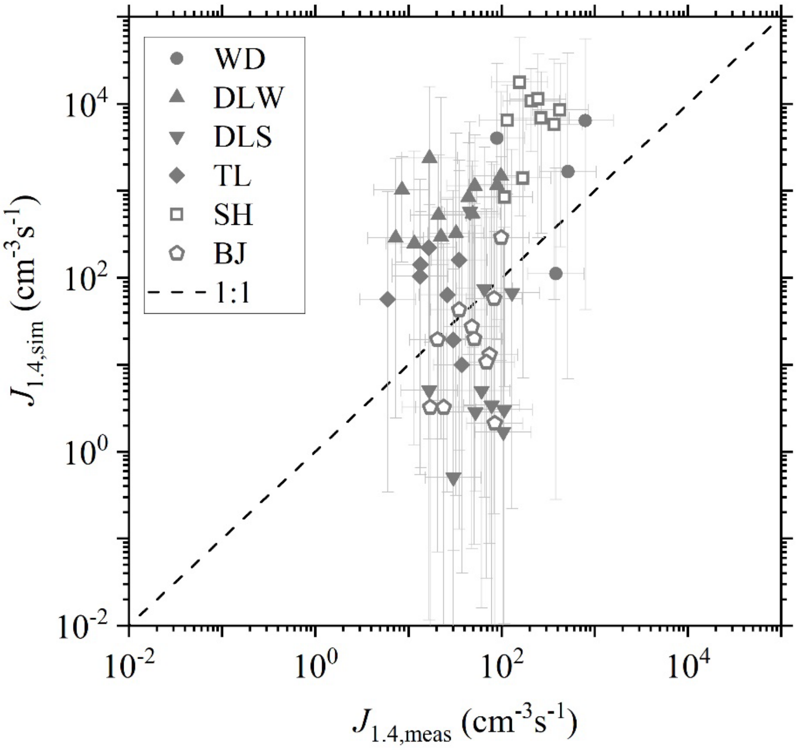

Figure S3: The comparison between $J_{1.4,meas}$ and $J_{1.4,sim}$. Horizontal and vertical error bars connected with each symbol indicate the uncertainties of x-axis and y-axis, respectively.

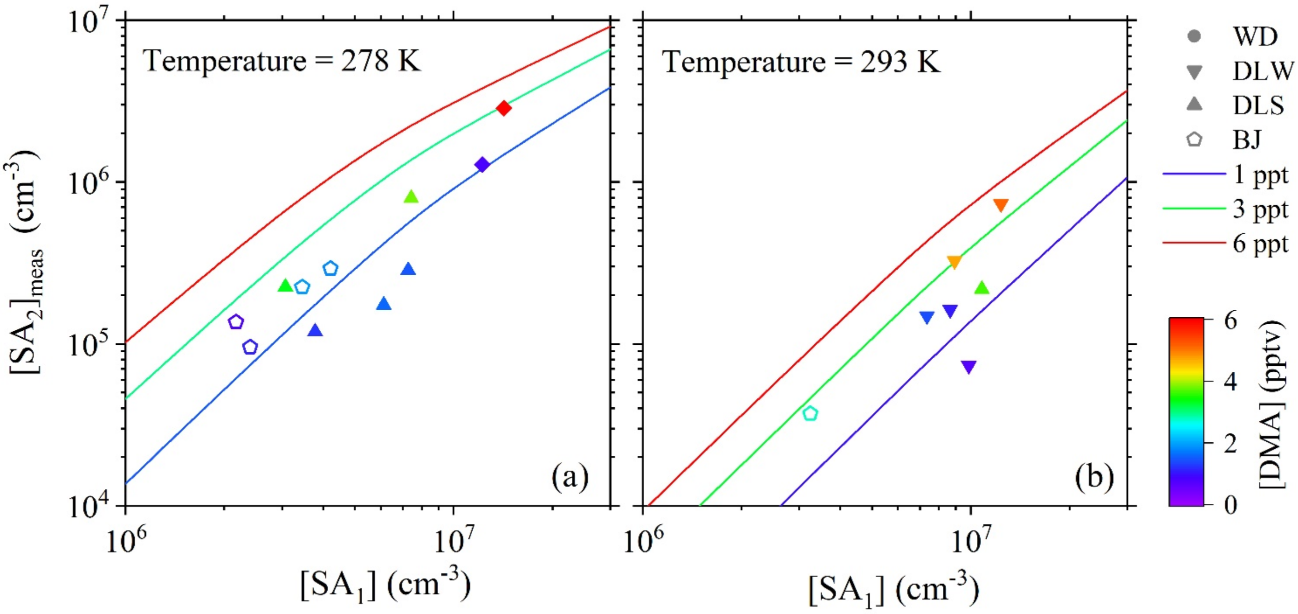

Figure S4: [SA$_2$]$_{meas}$ as a function of [SA$_1$] under a [DMA] gradient in two temperature ranges, 278±3 K and 293±3 K. Each temperature rang is indicated by its median value. The simulated lines are calculated by the discrete-sectional model the median value of the temperature range, i.e., 278 K or 293 K. [DMA] for the simulated lines is its median value (0.017 s^{-1}) in all NPF events.

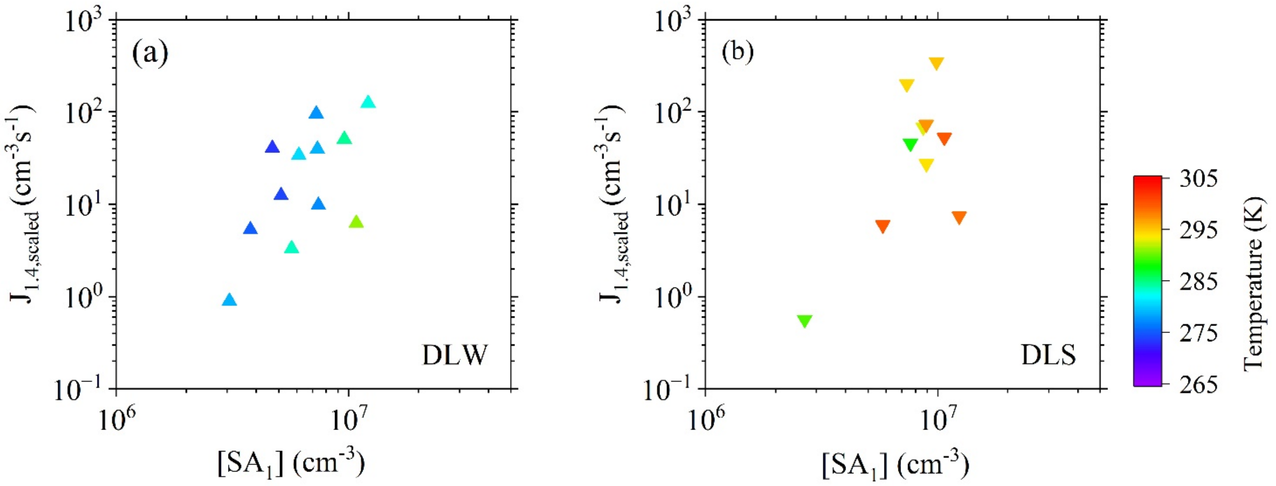

Figure S5: $J_{1.4,scaled}$ as a function of SA concentration under the temperature gradient in (a) winter and (b) spring campaigns at Dianshan Lake (DLW and DLS).

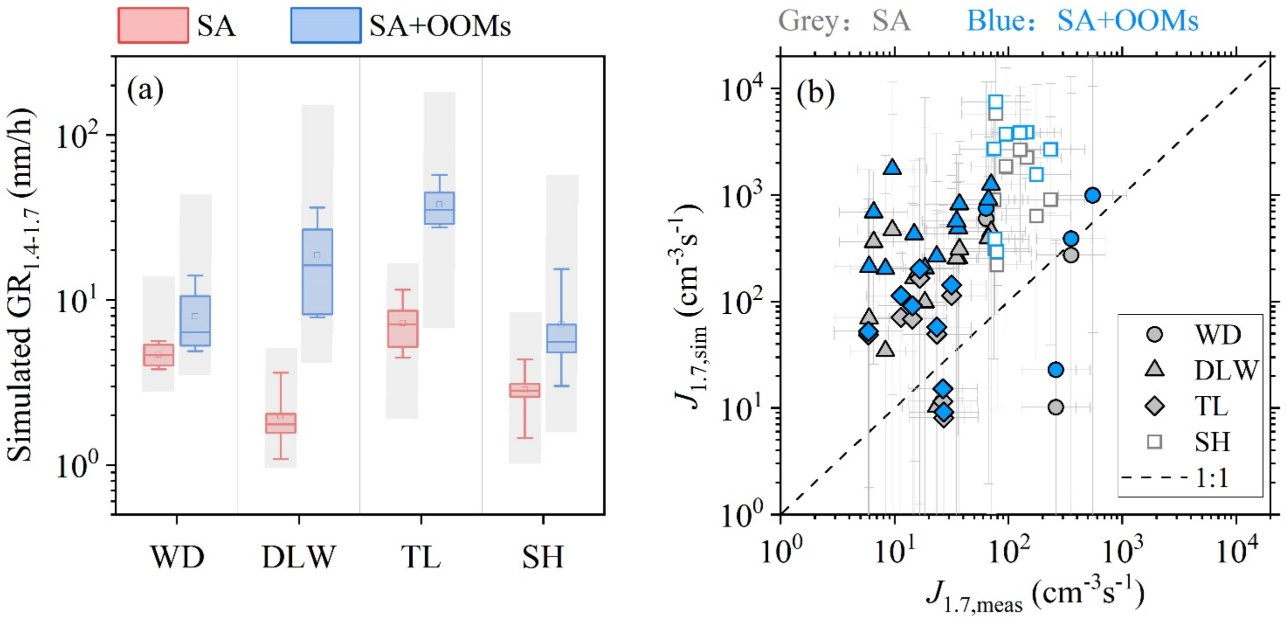

Figure S6: The comparison of simulated GR$_{1.4\text{-}1.7}$ contributed by SA and its clusters (i.e. SA in the legend), as well as SA and its clusters plus OOMs in different campaigns. The transverse lines and square markers inside the boxes indicate mean values and median values, respectively. The bottom and top edges of the box indicate the 25th and 75th percentiles, respectively. The bottom and top edges of the whisker lines outside of the boxes indicate the 10th and 90th percentiles, respectively. The shade boxes indicate the ranges of uncertainties.

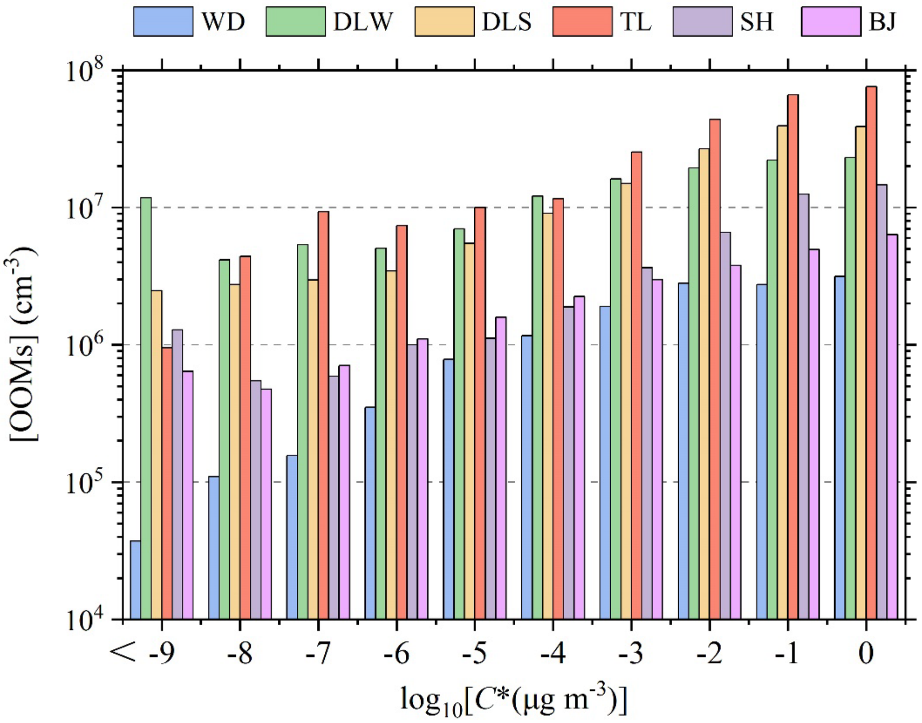

Figure S7: Comparison of volatility distribution of observed OOMs. Bars indicate the median values during NPF periods. OOMs with $\log_{10}[C^*(\mu g\ m^{-3})] \leq -9$ are merged into the group of bars on the far right. 160

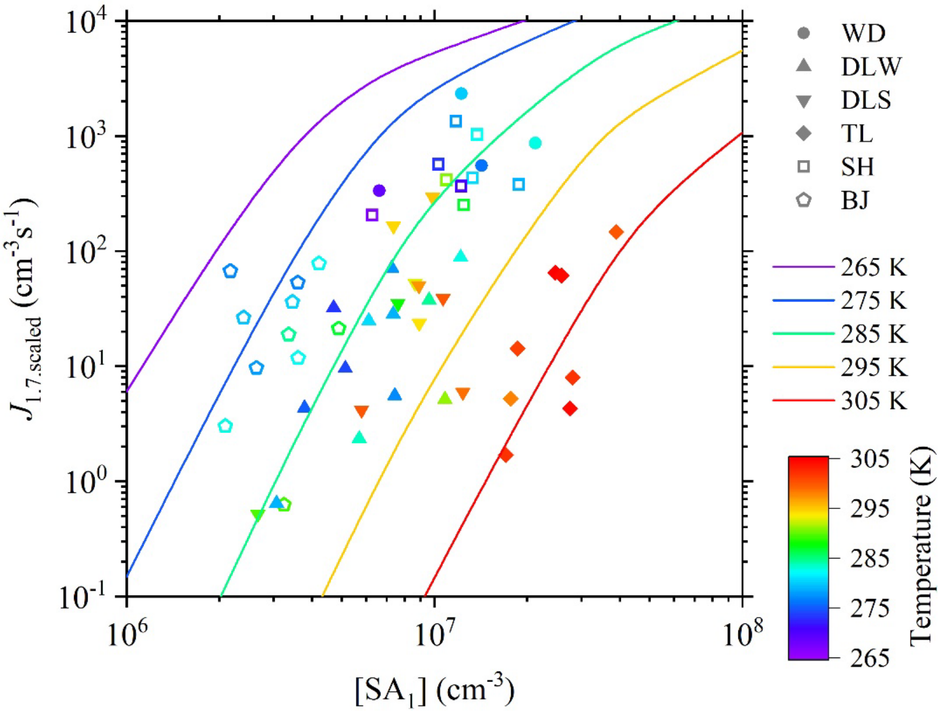

Figure S8: $J_{1.7,\text{scaled}}$ as a function of [SA_1] under the temperature gradient. Each symbol indicates one NPF event with a time resolution of 30 min, which was selected when $J_{1.7,\text{meas}}$ reaches maximum. [DMA], CS and P for the simulated lines by the discrete-sectional model are their median values in all NPF events, i.e., 0.017 s^{-1} ,2.3 pptv and 0.67, respectively. To visualize the effect of temperature, the color of the simulated line corresponds to the color bar. 165

References

Bianchi, F., Trostl, J., Junninen, H., Frege, C., Henne, S., Hoyle, C. R., Molteni, U., Herrmann, E., Adamov, A., Bukowiecki, N., Chen, X., Duplissy, J., Gysel, M., Hutterli, M., Kangasluoma, J., Kontkanen, J., Kuerten, A., Manninen, H. E., Muench, S., Perakyla, O., Petaja, T., Rondo, L., Williamson, C., Weingartner, E., Curtius, J., Worsnop, D. R., Kulmala, M., Dommen, J., and Baltensperger, U.: New particle formation in the free troposphere: A question of chemistry and timing, Science, 352, 1109–1112, https://doi.org/10.1126/science.aad5456, 2016.

Cai, R. and Jiang, J.: A new balance formula to estimate new particle formation rate: reevaluating the effect of coagulation scavenging, Atmos. Chem. Phys., 17, 12659–12675, https://doi.org/10.5194/acp-17-12659-2017, 2017.

Cai, R., Yan, C., Yang, D., Yin, R., Lu, Y., Deng, C., Fu, Y., Ruan, J., Li, X., Kontkanen, J., Zhang, Q., Kangasluoma, J., Ma, Y., Hao, J., Worsnop, D. R., Bianchi, F., Paasonen, P., Kerminen, V.-M., Liu, Y., Wang, L., Zheng, J., Kulmala, M., and Jiang, J.: Sulfuric acid-amine nucleation in urban Beijing, Atmos. Chem. Phys., 21, 2457–2468, https://doi.org/10.5194/acp-21-2457-2021, 2021.

Caudillo, L., Rorup, B., Heinritzi, M., Marie, G., Simon, M., Wagner, A. C., Mueller, T., Granzin, M., Amorim, A., Ataei, F., Baalbaki, R., Bertozzi, B., Brasseur, Z., Chiu, R., Chu, B., Dada, L., Duplissy, J., Finkenzeller, H., Carracedo, L. G., He, X.-C., Hofbauer, V., Kong, W., Lamkaddam, H., Lee, C. P., Lopez, B., Mahfouz, N. G. A., Makhmutov, V., Manninen, H. E., Marten, R., Massabo, D., Mauldin, R. L., Mentler, B., Molteni, U., Onnela, A., Pfeifer, J., Philippov, M., Piedehierro, A. A., Schervish, M., Scholz, W., Schulze, B., Shen, J., Stolzenburg, D., Stozhkov, Y., Surdu, M., Tauber, C., Tham, Y. J., Tian, P., Tome, A., Vogt, S., Wang, M., Wang, D. S., Weber, S. K., Welti, A., Wang, Y., Wu, Y., Zauner-Wieczorek, M., Baltensperger, U., El Haddad, I., Flagan, R. C., Hansel, A., Hoehler, K., Kirkby, J., Kulmala, M., Lehtipalo, K., Moehler, O., Saathoff, H., Volkamer, R., Winkler, P. M., Donahue, N. M., Kuerten, A., and Curtius, J.: Chemical composition of nanoparticles from α-pinene nucleation and the influence of isoprene and relative humidity at low temperature, Atmos. Chem. Phys., 21, 17099–17114, https://doi.org/10.5194/acp-21-17099-2021, 2021.

Donahue, N. M., Epstein, S. A., Pandis, S. N., and Robinson, A. L.: A two-dimensional volatility basis set: 1. organic-aerosol mixing thermodynamics, Atmos. Chem. Phys., 11, 3303–3318, https://doi.org/10.5194/acp-11-3303-2011, 2011.

Epstein, S. A., Riipinen, I., and Donahue, N. M.: A semiempirical correlation between enthalpy of vaporization and saturation concentration for organic aerosol, Environ. Sci. Technol., 44, 743–748, https://doi.org/10.1021/es902497z, 2010.

Freshour, N. A., Carlson, K. K., Melka, Y. A., Hinz, S., Panta, B., and Hanson, D. R.: Amine permeation sources characterized with acid neutralization and sensitivities of an amine mass spectrometer, Atmos. Meas. Tech., 7, 3611–3621, https://doi.org/10.5194/amt-7-3611-2014, 2014.

Ge, P., Luo, G., Huang, W., Xie, H., Chen, J., and Luo, Y.: Theoretical study of the hydration effects on alkylamine and alkanolamine clusters and the atmospheric implication, Chemosphere, 243, 125323, https://doi.org/10.1016/j.chemosphere.2019.125323, 2020.

Han, J., Wang, L., Zhang, H., Su, Q., Zhou, X., and Liu, S.: Determinant factor for thermodynamic stability of sulfuric acid–amine complexes, J. Phys. Chem. A, 124, 10246–10257, https://doi.org/10.1021/acs.jpca.0c07908, 2020.

Kulmala, M., Kontkanen, J., Junninen, H., Lehtipalo, K., Manninen, H. E., Nieminen, T., Petaja, T., Sipila, M., Schobesberger, S., Rantala, P., Franchin, A., Jokinen, T., Jarvinen, E., Aijala, M., Kangasluoma, J., Hakala, J., Aalto, P. P., Paasonen, P., Mikkila, J., Vanhanen, J., Aalto, J., Hakola, H., Makkonen, U., Ruuskanen, T., Mauldin, R. L., Duplissy, J., Vehkamaki, H., Back, J., Kortelainen, A., Riipinen, I., Kurten, T., Johnston, M. V., Smith, J. N., Ehn, M., Mentel, T. F., Lehtinen, K. E. J., Laaksonen, A., Kerminen, V.-M., and Worsnop, D. R.: Direct observations of atmospheric aerosol nucleation, Science, 339, 943–946, https://doi.org/10.1126/science.1227385, 2013.

Kürten, A., Li, C., Bianchi, F., Curtius, J., Dias, A., Donahue, N. M., Duplissy, J., Flagan, R. C., Hakala, J., Jokinen, T., Kirkby, J., Kulmala, M., Laaksonen, A., Lehtipalo, K., Makhmutov, V., Onnela, A., Rissanen, M. P., Simon, M., Sipilä, M., Stozhkov, Y., Tröstl, J., Ye, P., and McMurry, P. H.: New particle formation in the sulfuric acid–dimethylamine–water system: reevaluation of CLOUD chamber measurements and comparison to an aerosol nucleation and growth model, Atmos. Chem. Phys., 18, 845–863, https://doi.org/10.5194/acp-18-845-2018, 2018.

Li, C., Li, Y., Li, X., Cai, R., Fan, Y., Qiao, X., Yin, R., Yan, C., Guo, Y., Liu, Y., Zheng, J., Kerminen, V.-M., Kulmala, M., Xiao, H., and Jiang, J.: Comprehensive simulations of new particle formation events in Beijing with a cluster dynamics-multicomponent sectional model, Atmos. Chem. Phys., 23, 6879–6896, https://doi.org/10.5194/acp-23-6879-2023, 2023.

Li, X., Li, Y., Cai, R., Yan, C., Qiao, X., Guo, Y., Deng, C., Yin, R., Chen, Y., Li, Y., Yao, L., Sarnela, N., Zhang, Y., Petaja, T., Bianchi, F., Liu, Y., Kulmala, M., Hao, J., Smith, J. N., and Jiang, J.: Insufficient condensable organic vapors lead to slow growth of new particles in an urban environment, 56, 9936–9946, Environ. Sci. Technol., https://doi.org/10.1021/acs.est.2c01566, 2022.

Mohr, C., Thornton, J. A., Heitto, A., Lopez-Hilfiker, F. D., Lutz, A., Riipinen, I., Hong, J., Donahue, N. M., Hallquist, M., Petäjä, T., Kulmala, M., and Yli-Juuti, T.: Molecular identification of organic vapors driving atmospheric nanoparticle growth, Nat. Commun., 10, 4442, https://doi.org/10.1038/s41467-019-12473-2, 2019.

Myllys, N., Kubečka, J., Besel, V., Alfaouri, D., Olenius, T., Smith, J. N., and Passananti, M.: Role of base strength, cluster structure and charge in sulfuric-acid-driven particle formation, Atmos. Chem. Phys., 19, 9753–9768, https://doi.org/10.5194/acp-19-9753-2019, 2019.

Olenius, T., Halonen, R., Kurten, T., Henschel, H., Kupiainen-Maata, O., Ortega, I. K., Jen, C. N., Vehkamaki, H., and Riipinen, I.: New particle formation from sulfuric acid and amines: Comparison of monomethylamine, dimethylamine, and trimethylamine, J. Geophys. Res.-Atmos., 122, 7103–7118, https://doi.org/10.1002/2017JD026501, 2017.

Ortega, I. K., Kupiainen, O., Kurtén, T., Olenius, T., Wilkman, O., McGrath, M. J., Loukonen, V., and Vehkamäki, H.: From quantum chemical formation free energies to evaporation rates, Atmos. Chem. Phys., 12, 225–235, https://doi.org/10.5194/acp-12-225-2012, 2012.

Qiao, X., Yan, C., Li, X., Guo, Y., Yin, R., Deng, C., Li, C., Nie, W., Wang, M., Cai, R., Huang, D., Wang, Z., Yao, L., Worsnop, D. R., Bianchi, F., Liu, Y., Donahue, N. M., Kulmala, M., and Jiang, J.: Contribution of atmospheric oxygenated organic compounds to particle growth in an urban environment, Environ. Sci. Technol., 55, 13646–13656, https://doi.org/10.1021/acs.est.1c02095, 2021.

Riccobono, F., Schobesberger, S., Scott, C. E., Dommen, J., Ortega, I. K., Rondo, L., Almeida, J., Amorim, A., Bianchi, F., Breitenlechner, M., David, A., Downard, A., Dunne, E. M., Duplissy, J., Ehrhart, S., Flagan, R. C., Franchin, A., Hansel, A., Junninen, H., Kajos, M., Keskinen, H., Kupc, A., Kürten, A., Kvashin, A. N., Laaksonen, A., Lehtipalo, K., Makhmutov, V., Mathot, S., Nieminen, T., Onnela, A., Petäjä, T., Praplan, A. P., Santos, F. D., Schallhart, S., Seinfeld, J. H., Sipilä, M., Spracklen, D. V., Stozhkov, Y., Stratmann, F., Tomé, A., Tsagkogeorgas, G., Vaattovaara, P., Viisanen, Y., Vrtala, A., Wagner, P. E., Weingartner, E., Wex, H., Wimmer, D., Carslaw, K. S., Curtius, J., Donahue, N. M., Kirkby, J., Kulmala, M., Worsnop, D. R., and Baltensperger, U.: Oxidation products of biogenic emissions contribute to nucleation of atmospheric particles, Science, 344, 717–721, https://doi.org/10.1126/science.1243527, 2014.

Troestl, J., Chuang, W. K., Gordon, H., Heinritzi, M., Yan, C., Molteni, U., Ahlm, L., Frege, C., Bianchi, F., Wagner, R., Simon, M., Lehtipalo, K., Williamson, C., Craven, J. S., Duplissy, J., Adamov, A., Almeida, J., Bernhammer, A.-K., Breitenlechner, M., Brilke, S., Dias, A., Ehrhart, S., Flagan, R. C., Franchin, A., Fuchs, C., Guida, R., Gysel, M., Hansel, A., Hoyle, C. R., Jokinen, T., Junninen, H., Kangasluoma, J., Keskinen, H., Kim, J., Krapf, M., Kuerten, A., Laaksonen, A., Lawler, M., Leiminger, M., Mathot, S., Moehler, O., Nieminen, T., Onnela, A., Petaejae, T., Piel, F. M., Miettinen, P., Rissanen, M. P., Rondo, L., Sarnela, N., Schobesberger, S., Sengupta, K., Sipila, M., Smith, J. N., Steiner, G., Tome, A., Virtanen, A., Wagner, A. C., Weingartner, E., Wimmer, D., Winkler, P. M., Ye, P., Carslaw, K. S., Curtius, J., Dommen, J., Kirkby, J., Kulmala, M., Riipinen, I., Worsnop, D. R., Donahue, N. M., and Baltensperger, U.: The role of low-volatility organic compounds in initial particle growth in the atmosphere, Nature, 533, 527–531, https://doi.org/10.1038/nature18271, 2016.

Xiao, M., Hoyle, C. R., Dada, L., Stolzenburg, D., Kuerten, A., Wang, M., Lamkaddam, H., Garmash, O., Mentler, B., Molteni, U., Baccarini, A., Simon, M., He, X.-C., Lehtipalo, K., Ahonen, L. R., Baalbaki, R., Bauer, P. S., Beck, L., Bell, D., Bianchi, F., Brilke, S., Chen, D., Chiu, R., Dias, A., Duplissy, J., Finkenzeller, H., Gordon, H., Hofbauer, V., Kim, C., Koenig, T. K., Lampilahti, J., Lee, C. P., Li, Z., Mai, H., Makhmutov, V., Manninen, H. E., Marten, R., Mathot, S., Mauldin, R. L., Nie, W., Onnela, A., Partoll, E., Petaja, T., Pfeifer, J., Pospisilova, V., Quelever, L. L. J., Rissanen, M., Schobesberger, S., Schuchmann, S., Stozhkov, Y., Tauber, C., Tham, Y. J., Tome, A., Vazquez-Pufleau, M., Wagner, A. C., Wagner, R., Wang, Y., Weitz, L., Wimmer, D., Wu, Y., Yan, C., Ye, P., Ye, Q., Zha, Q., Zhou, X., Amorim, A., Carslaw, K., Curtius, J., Hansel, A., Volkamer, R., Winkler, P. M., Flagan, R. C., Kulmala, M., Worsnop, D. R., Kirkby, J., Donahue, N. M., Baltensperger, U., El Haddad, I., and Dommen, J.: The driving factors of new particle formation and growth in the polluted boundary layer, Atmos. Chem. Phys., 21, 14275–14291, https://doi.org/10.5194/acp-21-14275-2021, 2021.